Feasibility of Phase Velocity Imaging Using Multi Frequency Oscillation-Shear Wave Elastography

Md Murad Hossain, Member, *IEEE*, and Elisa E. Konofagou, Fellow, *IEEE*

***Abstract*— Objective: To assess viscoelasticity, a pathologically relevant biomarker, shear wave elastography (SWE) generally uses phase velocity (PV) dispersion relationship generated via pulsed acoustic radiation force (ARF) excitation pulse. In this study, a multi-frequency oscillation (MFO)–excitation pulse with higher weight to higher frequencies is proposed to generate PV images via the generation of motion with energy concentrated at the target frequencies in contrast to the broadband frequency motion generated in pulsed SWE (PSWE). Methods: The feasibility of MFO-SWE to generate PV images at 100 to 1000 Hz in steps of 100 Hz was investigated by imaging 6 and 70 kPa inclusions with 6.5 and 10.4 mm diameter and *ex vivo* bovine liver with and without the presence of an aberration layer and chicken muscle *ex vivo*, and 4T1 mouse breast tumor, *in vivo* with comparisons to PSWE. Results: MFO-SWE-derived CNR was statistically higher than PSWE for 6 kPa (both with and without aberration) and 70 kPa (with aberration) inclusions and derived SNR of the liver was statistically higher than PSWE at higher frequency (600-1000 Hz). Quantitatively, at 600-1000 Hz, MFO-SWE improved CNR of inclusions (without and with) aberration on an average by (8.2 and 156) % and of the tumor by 122%, respectively, and improved SNR of the liver (without and with) aberration by (20.2 and 51.5) % and of chicken muscle by 72%, respectively compared to the PSWE. Conclusions and Significance: These results indicate the advantages of MFO-SWE to improve PV estimation at higher frequencies which could improve viscoelasticity quantification and feature delineation.**

***Index Terms*—Phase velocity, multi-frequency oscillation, shear wave elastography, viscoelasticity, liver, muscle, tumor.**

I. Introduction

The elasticity of tissue has a powerful diagnostic relevance and is associated with a broad spectrum of pathologies as the elasticity of tissue varies with microstructure, composition, histology, and biochemistry. Over the last three decades, several ultrasonic methods have been developed to interrogate the elasticity of tissue and applied to diagnose diseases [1]. Along with elasticity, the assessment of viscosity is gaining prominence as the soft tissue exhibits mechanical behaviors of both elastic solids and viscous fluids [2]. Ignoring viscosity not only induces bias in the assessment of elasticity [3], [4] but also overlooks diagnostically relevant information in the liver [5]–[8], cancer [9]–[11], musculoskeletal [12]–[14], renal [15], [16], and other applications [17], [18]. Due to the diagnostic relevance of viscoelasticity, several ultrasonic methods to assess these parameters have been developed. To assess viscoelasticity, a subset of these methods either use ARF-induced "on-axis" displacements [19]–[21] or shear wave propagation "off-axis" to the ARF [6], [22]–[29] or both [30], [31].

The "on-axis" ARF-based methods generally fit the displacements to the well-known materials models [19], [21] to assess qualitative or relative viscoelasticity which means the viscoelasticity of a target region is compared with a reference region. These methods generally provide better spatial resolution and higher penetration depth as "on-axis" displacements are evaluated.

In contrast to displacement-based methods, "off-axis" shear wave-based methods assess quantitative viscoelasticity in terms of shear wave dispersion and attenuation characteristics [6], [32], [33], shear elastic and viscous moduli [22], [32], [34]–[36], complex moduli [31], relaxation time constants [19], [37], and loss tangent moduli [31]. Further, viscoelasticity in terms of modulus can be estimated by fitting shear wave dispersion to a rheological model [6], [23], [29] or in a model-independent manner by measuring both shear wave dispersion and attenuation [22], [24]–[26].

While most of these methods represent viscoelasticity as a point measure, some recent methods reconstruct 2-D images of PV [28] or viscoelastic parameters [22], [27], [29], [36]. Budelli *et al.* used Supersonic Imaging-derived PV and attenuation with the assumption of cylindrical shear wave propagation to reconstruct images of storage and loss moduli [27]. Van Sloun, *et al.* fitted the shear wave motion dynamics to a Kelvin-Voigt model to map viscosity and shear wave velocity with assumptions of linear systems and planar shear wave propagation [36]. Bhatt *et al.* reconstructed viscosity images by measuring attenuation using a frequency shift method with an assumption of the constant shape parameter of a power spectrum amplitude [22]. Kijanka *et al.* used temporal frequency and wavenumber relationship to generate PV images via 2-D Fourier transform analysis of a sliding window of 3x3 to 6x6 mm^2 [28].

All these methods used a pulsed ARF to generate motion in the frequency range of 50-2000 Hz. Instead of using pulsed ARF, oscillatory motion can be generated at the target frequency by repeating a pulse ARF at a particular frequency [23] or modulating ARF duration [38], [39], or by modulating ARF amplitude [30], [40], [41]. The advantages of generating oscillatory motion are two-fold. First, the motion energy can be concentrated at the target frequency instead of the wide frequency range as the shear wave loses energy as it propagates due to diffraction and viscosity. Second, the target frequency can be easily filtered from the motion artifacts. However, these oscillatory motion-based methods have their pros and cons.

The generation of narrowband motion using amplitude-

This work was supported by NIH under Grant R01 CA228275 (Corresponding author: Elisa E. Konogagou). M. M. Hossain is with Department of Biomedical Engineering and E. E. Konofagou is with the Department of Biomedical Engineering and Radiology, Columbia University, New York, NY 10027 USA. (ek2191@columbia.edu).

modulated ARF requires either a mechanical vibrator [41] or focused ultrasound (FUS) transducer [30], [40] and then, a separate imaging ultrasound transducer is required to track the shear wave propagation. This makes the system very complex for diagnostic use and inaccessible to different organs. The main drawback of the repetition of a pulsed ARF at a particular frequency [23] is the generation of motion with amplitudes comparable between fundamental versus harmonic frequencies. As the wave energy is distributed over several harmonics, it may limit its application in a low SNR scenario. Sadeghi *et al*. used a single imaging transducer to generate oscillatory motion by modulating ARF duration and then, the tracking pulse was transmitted in between the discrete excitation pulse to track shear wave propagation [38]. While ARF duration modulation generates motion with a target frequency amplitude several times higher than harmonic frequencies, this method requires separate acquisition to collect PV at multiple frequencies which may be challenging in the clinical imaging scenario due to the long imaging time and difficulty in registering different frequency images if there are patients or sonographer hand movements. Note, PVs at multiple frequencies are needed to assess viscoelasticity. In addition, the authors evaluated the performance of their method in homogeneous phantoms only. To assess phase velocities at multiple frequencies simultaneously, Zheng *et al*. proposed an orthogonal frequency-based excitation pulse via pulse duration modulation which was generated using a FUS transducer, and then, an imaging transducer was used for tracking motion [42]. The limitations of the study were the use of a complex set-up consisting of two separate transducers to generate and track shear waves, the assessment of phase velocities as a point measure, and the experimental demonstration in a homogeneous phantom only without any validation of estimated PV.

Towards the goal of generating PV images at multiple frequencies simultaneously with a single imaging ultrasound transducer to facilitate data acquisition in clinical settings, this study investigates the use of a new method, called MFO-SWE which is extended from our previous preliminary work, published as a conference abstract [43]. The main innovation in MFO-SWE is the employment of a multi-frequency excitation and tracking pulse sequence in a single imaging transducer to generate and track shear wave motion at targeted several frequencies. The excitation pulse in MFO-SWE is generated via the sum of sinusoids with higher weights to higher frequencies and is then sampled to transmit tracking pulses interleaved with excitation pulses. A further innovation is the generation of PV images of phantom and biological tissues using the employed excitation and tracking pulse sequence. The objectives of this study are as follows. First, the feasibility of generating PV images at 100-1000 Hz is demonstrated using a novel MFO excitation pulse. Second, the performance of the proposed method is compared against PSWE-derived PV [29] and group velocity (GV) [44] by imaging inclusions in a calibrated phantom and *ex vivo* bovine liver with and without a presence of a phase aberration layer and *ex vivo* chicken muscle. Third, *in vivo*, feasibility of MFO-SWE is demonstrated by imaging a 4T1 breast cancer mouse tumor in comparison to PSWE.

II. Materials and Methods

A. MFO-SWE Excitation and Tracking Pulse Sequence

In MFO-SWE, the voltage in the ultrasound system (i.e., the pressure of the excitation pulse) was kept constant whereas the duration of the excitation pulse is varied to generate an amplitude-modulated ARF because variation in duration will generate excitation pulses with different intensities (or energies). To generate excitation and tracking pulse sequence in MFO-SWE, a continuous pulse is first generated as follows by summing sinusoids with an integer multiple of fundamental frequency f_L and higher weight to the higher frequencies:

$$ep_1(t) = \sum_{m=1}^{M_{sinusoid}} m^2 \times cos(2\pi m f_L t + \varphi_m) \quad where,\ \varphi_m = \begin{cases} \pi, & if\ m\ odd \\ 0, & if\ m\ even \end{cases} \tag{1}$$

where $M_{sinusoid}$ defines the total sinusoid or discrete frequency number and the multiplication term, m^2 gives larger weight to the higher frequency to account for the higher loss with frequency. The phase (φ_m) of sinusoids alternates between 0 and π to maximize the $ep_1(t)$ dynamic range to produce motion with a higher range. Note, $ep_1(t)$ contains both positive and negative values. However, the excitation pulse duration cannot be negative. To have only positive values, the following equation is used:

$$ep_2(t) = ep_1(t) - 1.25 \times \min(ep_1(t)) \tag{2}$$

where $min(ep_1(t))$ means a minimum of $ep_1(t)$. Note that a minimum of $ep_1(t)$ is a negative number. Therefore, (2) means an addition of a dc offset to $ep_1(t)$. Then, $ep_2(t)$ was rescaled so that the minimum and maximum of $ep_2(t)$ represent the minimum (100 µs) and maximum (300 µs) pulse duration. The rescaled $ep_2(t)$ i.e., $ep_{2r}(t)$ is then sampled as follows to transmit tracking pulses in between the N_{ep} discrete excitation pulses (see Fig. 1).

$$EP[n] = ep_{2r}(t) \times \sum_{n=1}^{N_{ep}} \delta(t - t_n) \tag{3}$$

where, δ is the Delta-Dirac function and t_n defines the nth discrete excitation pulse location in the time-axis. Compounded plane wave imaging was used as a tracking pulse for estimating excitation pulse-induced motion.

B. Phantom Experiments

The MFO-SWE with parameters in Table I is implemented in a Verasonics research system (Vantage 256, Verasonics Inc., Kirkland, WA, USA) equipped with an L7-4 transducer (Philips Healthcare, Andover, MA, USA) for imaging a commercially available elastic phantom (model 049A, CIRS, Norfolk, VA, USA). Two stepped-cylindrical inclusions with nominal Young's moduli of 6 and 70 kPa embedded in an 18 kPa background were imaged by submerging the phantom in water. For each stiffness, imaging was performed at 6.5 and 10.4 mm diameter inclusion cross-sections. To investigate the effect of the phase aberration on PV imaging, approximately 4

Table I
EXCITATION AND TRACKING PULSE PARAMETERS OF MULTI FREQUENCY OSCILLATION-SHEAR WAVE ELASTOGRAPHY (MFO-SWE) AND PULSED SWE (PSWE) USED IN IMAGING PHANTOMS, EXCISED BOVINE LIVER AND CHICKEN MUSCLE, AND IN VIVO BREAST CANCER MOUSE WITH LOUPAS PARAMETERS FOR DISPLACEMENT ESTIMATION.

Parameters	Phantom/Liver /Chicken	Mouse
Beam sequence parameters of MFO-SWE / PSWE		
Transducer	L7-4	L11-5
Bandwidth	58%	77%
Sampling frequency	31.25 MHz	62.5 MHz
Acoustic lens axial focus	25 mm	18 mm
Excitation pulse center frequency	4.0 MHz	5.0 MHz
Excitation pulse F-number	2.4/1.7/2.0	1.7
Tracking pulse center frequency	6.1 MHz	8.9 MHz
Compounded plane wave per tracking pulse	3	3
Reference tracking pulse number	10	10
Plane wave angle range	[-4°, 4°]	[-4°, 4°]
Compounded frame rate	5.3 /5.7/5.3 KHz	5.7 KHz
Excitation beam axial focus	32/25/18 mm	25 mm
MFO-SWE / PSWE frames per acquisition	2/3/2	2
Excitation beam lateral focus location	-12, 12 / -12, 0, 12/ -12, 12 mm	-7.5, 8.5 mm
MFO-SWE specific parameters		
Lowest oscillation frequency, f_L	100 Hz	100 Hz
Sinusoids number, $M_{sinusoid}$	10	10
Discrete excitation pulse duration	168-213 µs	154-216 µs
Cycle number, N_{cycle}	4	4
PSWE specific parameters		
Tracking compounded frame	175	175
Excitation pulse duration	350 µs	300 µs
Loupas displacement estimator parameters		
Interpolation factor	4	4
Kernel length	1010 µm	692 µm

mm pork abdominal layer (mainly skin and fat), purchased from the local store, was placed in between the transducer and phantom surface. The center of the inclusion was approximately 33 and 36 mm from the transducer surface without and with the presence of the aberration layer, respectively and the transducer was held in a steady position using a clamp.

For comparison, PSWE with parameters in Table I was performed using the same system immediately following MFO-SWE. For both PSWE and MFO-SWE, focused excitation and plane wave tracking beams were implemented. For each acquisition, 2 frames of PSWE and MFO-SWE were acquired by electronically translating the excitation beam lateral focus location from the left (-12.0 mm) to the right side (12.0 mm). The final PV was the average of PV images generated using left-to-right and right-to-left propagating shear waves at these two frames. By moving the transducer in the elevational direction, 7 repeated acquisitions of PSWE and MFO-SWE were acquired at each inclusion. For delineating the inclusion boundary, one high-resolution spatially-matched B-mode image was acquired using 61 angles compounded plane wave with a range from -15° to 15° preceding each MFO-SWE sequence.

C. Ex Vivo Bovine Liver and Chicken Muscle Experiments

Both PSWE and MFO-SWE with parameters in Table I were performed on the *ex vivo* bovine liver and chicken breast sample. Both bovine liver and chicken breast samples were purchased from a local grocery store. Both samples were kept refrigerated after collection. On the day of the experiment, samples were removed from the refrigerator and sat at room temperature for 3 hours before being placed in a water bath for imaging. For the liver, a pork abdominal layer was placed in between the transducer and liver surface to investigate the effect of the aberration layer, and 7 repeated acquisitions of PSWE and MFO-SWE were acquired by translating the transducer elevationally. At each location, 3 frames were collected with excitation beam lateral focus locations at -12.0, 0.0, and 12.0 mm. For imaging chicken muscle, PSWE and MFO-SWE were performed both in the longitudinal and transverse direction by manually orienting the transducer, and the excitation beam lateral focus location was set to -12.0 and 12.0 mm at 1st and 2nd frames, respectively. Similar to the phantom experiment, spatially matched high-resolution B-mode images were also collected.

D. In Vivo Breast Cancer Mouse Experiment

In vivo, PSWE and MFO-SWE imaging of an orthotopic, 4T1 breast cancer mouse tumor (N=1) was performed using the ultrasound system with an L11-5 linear array (Verasonics Inc., Kirkland, WA, USA) (Table I). The protocol for the cancer induction and imaging was reviewed and approved by the Columbia University Irving Medical Center Institutional Animal Care and Use Committee. 10^5 4T1 breast cancer cells were injected into the 4th inguinal mammary fat pad of the eight to ten-week-old female BALB/c mice (Jackson Laboratory) [45], [46], and imaging was performed at 27-day post-injection of cancer cells. The anesthetized mice (1- 2% isoflurane in oxygen) were imaged by placing the mice in a supine position with beam lateral focus locations at -7.5 and 8.5 mm.

E. PSWE and MFO-SWE Data Processing

The method, described in [28], was adapted to generate PV images at 100 to 1000 Hz in steps of 100 Hz after transferring PSWE and MFO-SWE channel data from the Verasonics workstation to the computational workstation for offline processing. All processing steps, summarized in Fig. 1, were identical between PSWE and MFO-SWE and performed in MATLAB (MathWorks Inc., Natick, MA, USA). First, the Loupas estimator [50] (Table I) was applied to the delay-and-sum beamforming [49] constructed radiofrequency (RF) data to calculate inter-frame displacements, which yielded in a 3-D dataset (axial x lateral x time) describing axial particle motion over time. Second, a 2-D spline interpolation (*interp2* function) was applied to the 2-D motion data at each time point to convert the anisotropic pixel size (0.04 x 0.6 mm^2) to an isotropic pixel size of 0.1 mm. Third, at each pixel temporal motion is converted to the temporal frequency domain using 1-D Fourier transform (*fft* function), and then, 2-D spatial

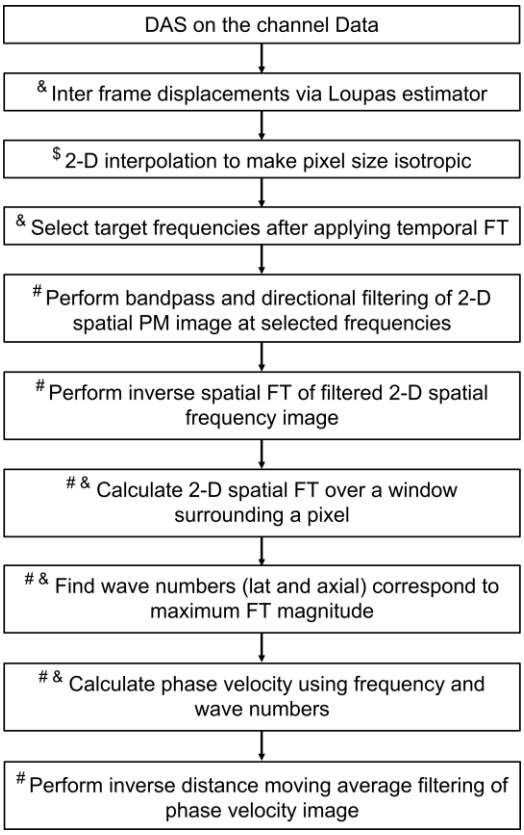

Fig 1: Data processing steps employed to generate phase velocity (PV) image at 100-1000 Hz using both PSWE and MFO-SWE methods. Steps marked by &, $, and # mean steps are repeated for each pixel, time point, and frequency, respectively. Note, some steps are repeated for more than one case. DAS = Dealy-and-sum; FT = Fourier transform; PM = Particle motion;

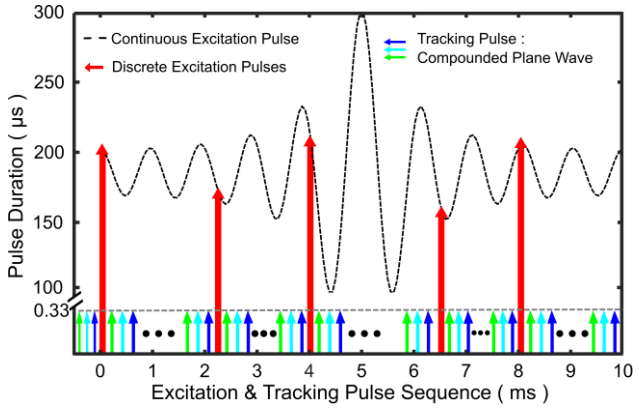

Fig 2: Continuous (dotted black) and discrete (red arrow) excitation pulse with 100 to 1000 Hz in steps of 100 Hz frequencies with interleaved compounded plane waves tracking pulses (red, blue, and green arrows). Y-axis contains a break to accommodate the difference in excitation and tracking pulse duration.

motion images at 100-1000 Hz were selected. Fourth, 2-D Fourier transform (*fft2* function) was applied to convert the 2-D spatial motion image at each frequency to 2-D spatial frequency (k_{lat}, k_{axial}) image, and then, 2nd-order Butterworth bandpass and directional filtering were applied to each 2-D spatial frequency image using the method described in [47]. The power of the spatially directional component of the directional filter was 2, which controls the angular width of the filter. The passband of the bandpass filter at each frequency was calculated by setting lower and higher PV to 0.2 and 10 ms^{-1}, respectively. Note, if the excitation beam lateral focus location is left (negative lateral number) or right side (positive lateral number) then left to right or right to left propagating shear wave, respectively was selected using the directional filter. However, if the excitation beam lateral focus location was at the center of the lateral field of view, then both shear waves were used. Fifth, 2-D inverse Fourier transform (*ifft2* function) was applied to convert filtered 2-D spatial frequency image at each temporal frequency to filtered 2-D spatial motion image. Sixth, at each pixel, a 2-D Fourier transform was performed over a 2-D window (4 x 4 mm^2) surrounding a pixel to transform spatial motion to spatial frequency, and then, lateral and axial wave-numbers corresponding to the maximum Fourier transform amplitude were found. This step is repeated for all pixels and temporal frequencies and the following equation was used for PV calculation.

$$PV = \frac{2\,\pi\, f_t}{\sqrt{k^2_{axial,\ max} + k^2_{lat,\ max}}} \tag{4}$$

where f_t and $k_{lat,\ max}$, and $k_{axial,\ max}$ represents temporal frequency and lateral and axial wave numbers correspond to the maximum FT amplitude. Sixth, the generated PV image at each temporal frequency was smoothed out using a 2-D inverse distance moving average filter with a window size of 3x3 mm^2. As multiple frames of PSWE or MFO-SWE data (Table I) were acquired, these steps were repeated to generate PV images at each frame. Then, the final PV image at each frequency is the average of the PV image at each frame. It took 7 min to process data from performing the delay-and-sum beamforming to generating the final PV images at 100-1000 Hz using a 2.2 GHz Intel Xeon Platinum processor with a 20 cores processor. The computational time can be reduced by implementing data processing pipelines (Fig. 1) in CUDA GPU.

For comparison, PSWE data was also used to calculate GV using a cross-correlation-based method [44] with a window and patch size of 3.4 x 3.4 mm^2. Similar to the PV calculation, 2nd-order Butterworth bandpass and directional filter were applied and the final GV image is the average of GV at each frame.

F. Image Quality Metrics

The performance of MFO-SWE and PSWE-derived PV and GV images of inclusions and tumor were compared in terms of contrast to noise ratio (CNR). CNR was computed as $|\mu_{INC} - \mu_{BKD}| / \sqrt{(\sigma^2_{INC} + \sigma^2_{BKD})}$ where μ and σ are the median and standard deviation of PV in the region of interest (ROI) in inclusions (INC) and background (BKD) [48] (see Fig. 4). The median was used so that the CNR calculation is robust to outliers. However, the signal-to-noise ratio (SNR), calculated as μ/σ, was used to compare PSWE and MFO-SWE-generated PV images of the liver and chicken muscle.

G. Statistical Analysis

All statistical analyses were performed in MATLAB. For

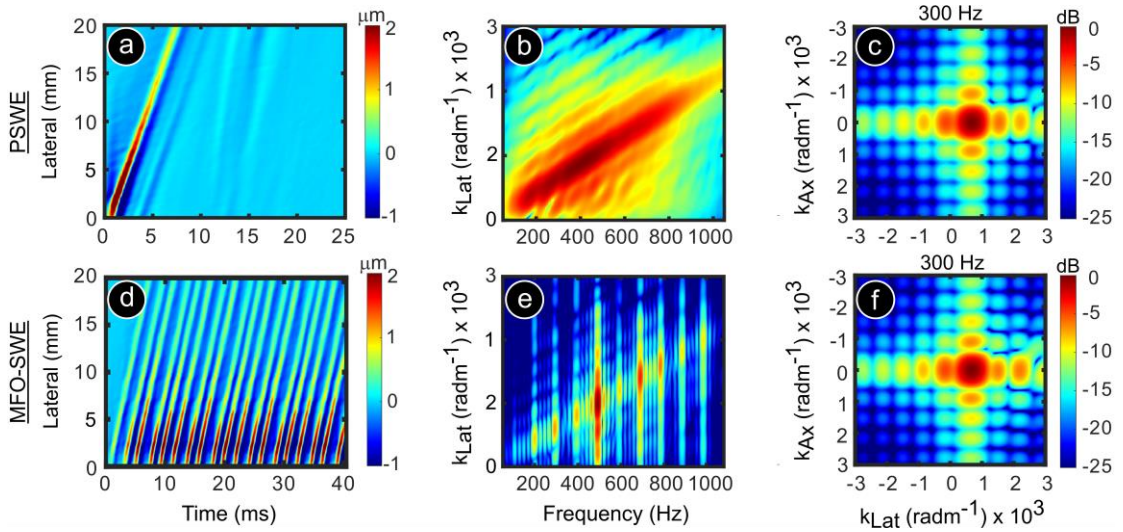

Fig 3: PSWE and MFO-SWE-derived image of (a, d) particle motion in the lateral-time axis, (b, e) spatial-temporal frequency of particle motion, and (c, f) lateral-axial spatial frequency of a homogeneous part of the phantom. k_{Lat} and k_{Ax} mean spatial wave number in the lateral and axial direction. The center and right columns have the same colorbar.

evaluating inclusion imaging performance, 16 (diameter, N = 2, stiffness, N = 2, PSWE and MFO-SWE, N=2, with and without aberration, N=2) separate Kruskal-Wallis tests (*kruskalwallis* function), were carried out to compare PSWE and MFO-SWE-derived CNRs at 100-1000 Hz. If any group was statistically significant, a two-sample Wilcoxon signed rank-sum test (*signrank* function) was used to find which frequencies were statistically significant from the frequency that generated the highest median CNR. As the objective is to maximize CNR for inclusion imaging, maximum CNR was compared between PSWE and MFO-SWE using the Wilcoxon signed rank-sum test. For liver imaging, PSWE and MFO-SWE-derived PV and SNR at each frequency were compared using the Wilcoxon signed rank-sum test. For all the analyses, the statistical significance was based on $p < 0.05$.

III. Results

Fig. 2 shows continuous (dotted line) and discrete (red arrow) multi-frequency excitation pulse with $M_{sinusoid} = 10$ and 1 cycle of f_L = 100 Hz. Therefore, the continuous pulse predominantly contains frequencies from 100 to 1000 Hz in steps of 100 Hz (equ (1)). The Y-axis in Fig. 2 is shown in terms of the pulse duration to underline the change in pulse duration in excitation pulse over time. Instead of changing the voltage to generate amplitude-modulated-ARF, the MFO-SWE methods modulate the excitation pulse duration to generate amplitude-modulated-ARF. Note that, pulse intensity (i.e., ARF magnitude) is directly proportional to the pulse duration. While the range of continuous excitation pulse duration is from 100 to 300 μs, the range of discrete excitation pulse duration is from 168 to 212.5 μs. The 3 compound plane waves (green, cyan, and blue arrows) tracking pulses were transmitted in between the discrete excitation pulse. Note that the tracking pulse (i.e., typical 2-cycle B-mode pulse) duration was fixed, unlike the discrete excitation pulse duration. The compounded plane wave tracking pulse number depends on the frame rate and time between two discrete excitation pulses. As an example, the tracking pulse number was 13 versus 9 in-between 1st and 2nd versus 2nd and 3rd discrete excitation pulses. While 1 cycle of MFO pulse is shown in Fig. 2, data were collected using 4 cycles of MFO pulse (Table I).

Fig. 3 compares PSWE and MFO-SWE in terms of lateral-temporal particle motion (panels: a and d), spatial-temporal frequency of particle motion (panels: b and e), and lateral-axial spatial frequency at f_t = 300 Hz (panels: c and f). The images were generated by imaging a homogenous part of the phantom. As 5 discrete excitation pulses per period were transmitted, 5 shear wavefronts per period (10 ms) were also visible in the MFO-SWE image (panel d). However, a single shear wave front is present in the PSWE image in panel (a). As a single impulsive excitation pulse was transmitted in PSWE, the generated temporal frequency was in the broadband range with magnitude decreased with frequency (panel b). Note, the magnitude was lower around 50 Hz due to the application of bandpass and directional filtering. In contrast to PSWE, the energy of the particle motion in MFO-SWE was concentrated at 100 to 1000 Hz in steps of 100 Hz frequency with the highest magnitude at 500 Hz (panel e). This result indicates that an MFO excitation pulse can be used to distribute the pulse energy at the target frequencies. The lateral-axial spatial frequency image at f_t = 300 Hz was similar for PSWE versus MFO-SWE (panel c versus f). The lateral and axial wavenumbers ($k_{lat,\ max}$, $k_{axial,\ max}$) correspond to the maximum Fourier transform magnitude was (690.4, 5.1) and (680.2, 5.1) $radm^{-1}$ which yielded PSWE and MFO-SWE-derived PV of 2.72 and 2.76 ms^{-1} at 300 Hz according to (4), respectively.

Fig. 4 shows representative B-mode, GV, and PV images at 100-1000 Hz derived by PSWE and MFO-SWE for 6.5 mm diameter, 6 kPa inclusion without and with the presence of an aberration layer. B-mode and GV images of both inclusions are shown side-by-side in the 1st row whereas PSWE and MFO-SWE derived PV images at each frequency are shown side-by-side for without (2nd and 3rd row) and with aberration (4th and 5th row). Six observations are notable. First, PV and

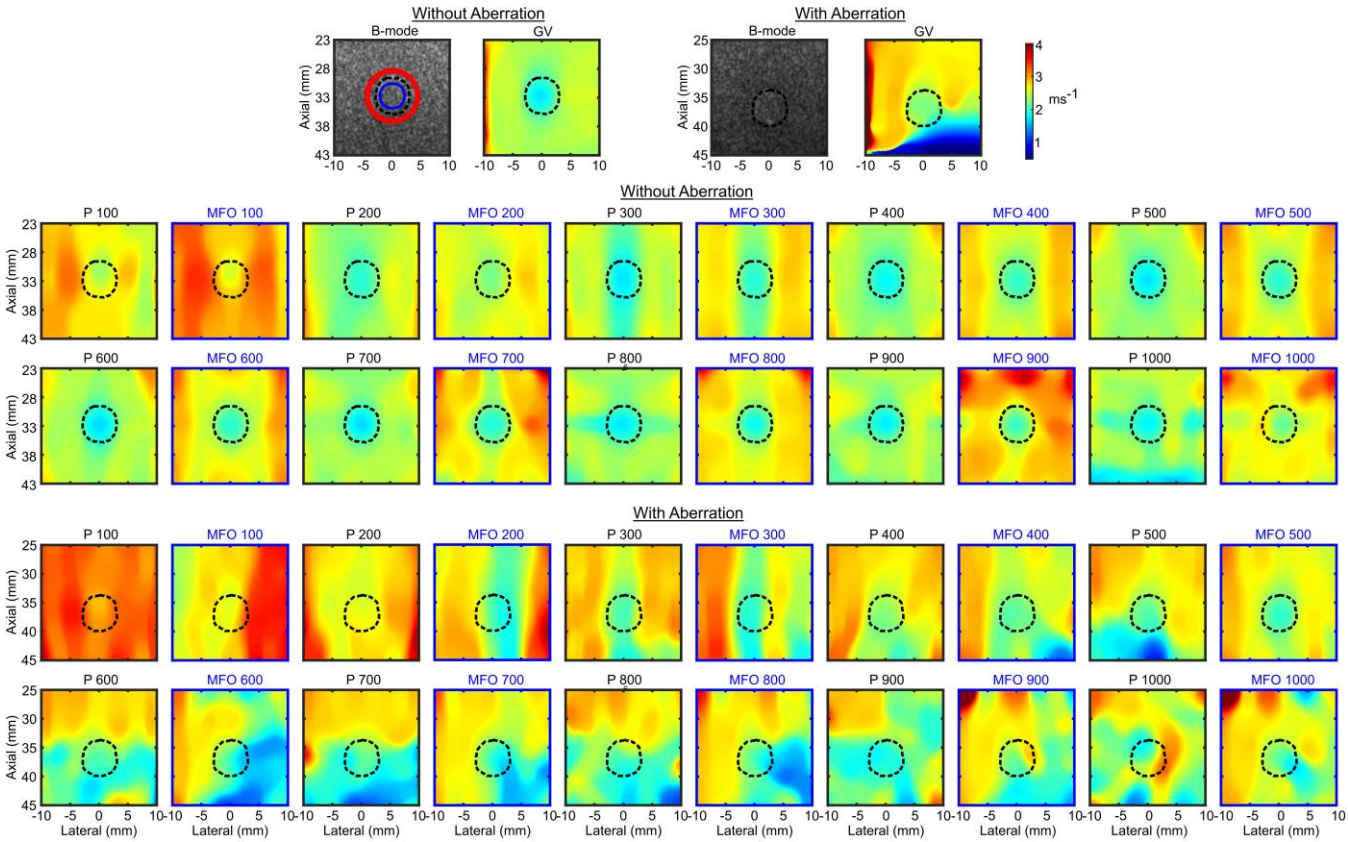

Fig 4, 6.5 mm diameter, 6 kPa inclusion: B-mode, PSWE-derived group velocity (GV), PSWE and MFO-SWE-derived phase velocity (PV) images at 100-1000 Hz of the inclusion with and without the presence of an aberrating layer. B-mode and GV images are shown side-by-side at the 1st row. PSWE (denote by P) and MFO-SWE (denote by MFO) - derived PV image at each frequency are shown side-by-side at (2nd, 3rd) and (4th, 5th) rows for without and with the aberrating layer, respectively. Note, the axial range is differnet for images without and with the aberrating layer. The border and title of PSWE and MFO-SWE-derived PV images are in black versus blue color for better distinction. Circular region-of-interest (blue and red contour in Bmode) is used to calculate CNR for comparing PSWE versus MFO-SWE whereas black dashed contour represents inclusion boundary. The colorbar applies to all GV and PV images.

GV were lower in inclusion compared to the background as the inclusion was softer than the background (6 versus 18 kPa). Second, higher (500-900 Hz) and lower (300-500 Hz) frequencies delineated inclusion better than other frequencies without and with the aberration layer, respectively irrespective of methods. Third, while there was no huge difference in delineating inclusions between PSWE and MFO-SWE without aberration, MFO-SWE clearly delineated inclusion with aberration better than PSWE, especially at 500 Hz. Fourth, PSWE-derived PV delineated inclusion better than GV without aberration whereas GV delineated inclusion better with aberration compared to PV. In contrast, MFO-SWE-derived PV delineated inclusions better than PSWE-derived GV for both cases of with or without aberration. This result indicates the advantage of distributing energy to target frequencies (equation (1)). Sixth, PV in background or inclusion did not significantly change with the frequency which indicates the primarily elastic nature of the phantom.

Similar to Fig. 4, representative B-mode, GV, and PV images at 100-1000 Hz derived by PSWE and MFO-SWE for 6.5 mm diameter, 70 kPa inclusion with and without aberration are demonstrated in Fig. 5. As the inclusion was stiffer than the background (70 versus 18 kPa), GV and PV in inclusion were higher than the background. The performance was similar between PSWE and MFO-SWE without aberration, MFO-SWE clearly delineated inclusion with aberration better than PSWE for frequency 700-1000 Hz. MFO-SWE-derived PV at 900-1000 Hz delineated inclusion better than PSWE-derived GV. The change in PV with respect to frequency was also minimal.

Fig.6 quantitatively compares the performance of GV, PSWE, and MFO-SWE-derived PV in delineating 4 different inclusions with and without aberration in terms of CNR. The CNR of inclusion in PV images varied with frequency, and maximum CNR was yielded at a different frequency for different inclusions and conditions. The maximum CNR yielded by (PSWE, MFO-SWE) for 6.5 mm 6 kPa, 10.4 mm 6 kPa, 6.5 mm 70 kPa, and 10.4 mm 70 kPa inclusions without aberration at (700, 600), (600, 600), (800, 800), (1000, 700) Hz and with aberration at (300, 500), (200, 500), (600, 1000), (500, 700) Hz respectively. The MFO-SWE-PV-derived maximum CNR was significantly higher than PSWE-PV and GV-derived CNR for both softer inclusions without and with aberration (except 10.4 mm 6 kPa with aberration: MFO-SWE-PV versus PSWE-GV, panels: a and b). PSWE-GV-derived CNR was significantly higher than MFO-SWE- and PSWE-PV-derived maximum CNR for both stiffer inclusions without aberration (panels: c and d). With aberration, MFO-

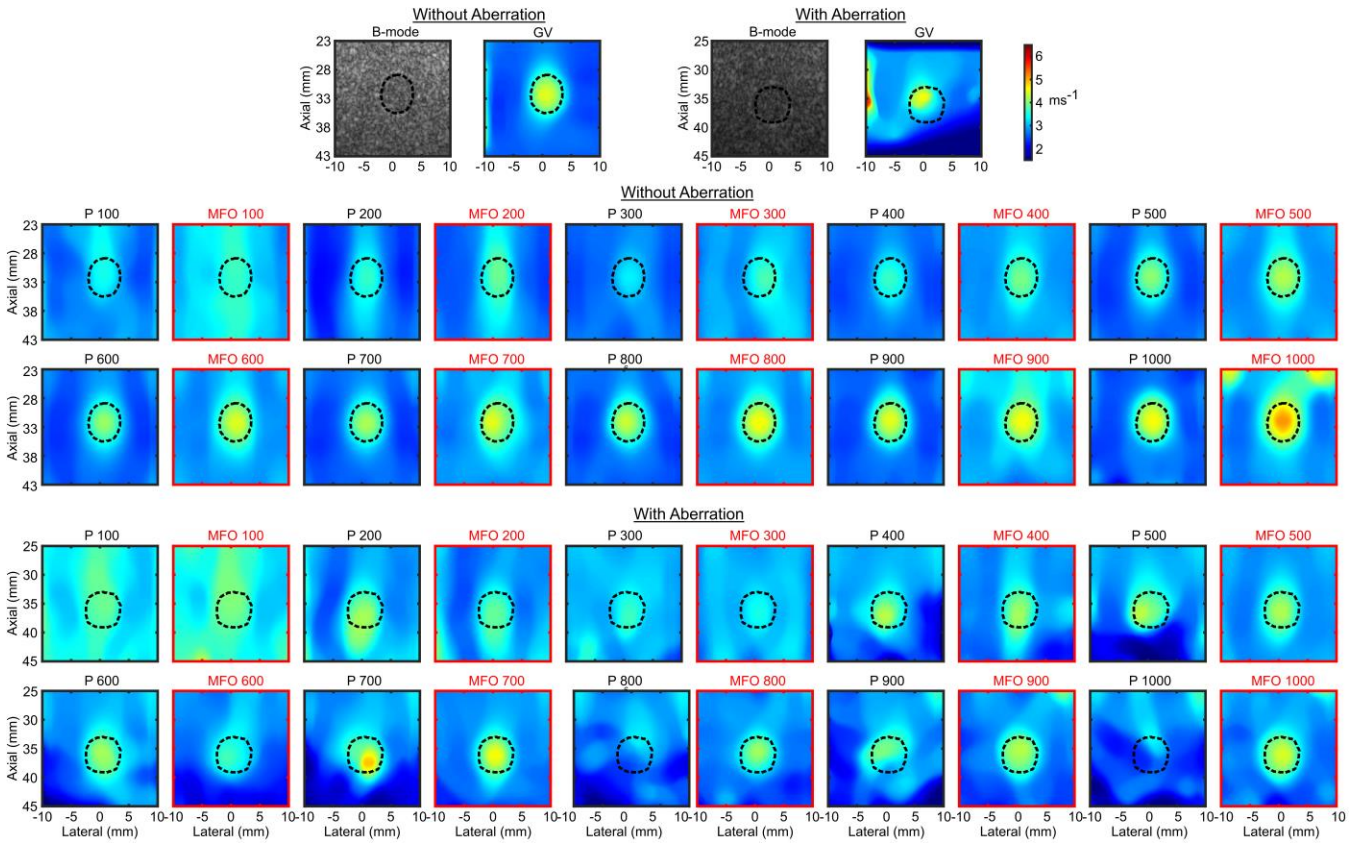

Fig 5, 6.5 mm diameter, 70 kPa inclusion: B-mode, PSWE-derived group velocity (GV), PSWE and MFO-SWE-derived phase velocity (PV) images at 100-1000 Hz of the inclusion with and without the presence of an aberrating layer. B-mode and GV images are shown side-by-side at the 1st row. PSWE (denote by P) and MFO-SWE (denote by MFO) - derived PV image at each frequency are shown side-by-side at (2nd, 3rd) and (4th, 5th) rows for without and with the aberrating layer, respectively. Note, the axial range is differnet for images without and with the aberrating layer. The border and title of PSWE and MFO-SWE-derived PV images are in black versus red color for better distinction. Black dashed contour represents inclusion boundary. The colorbar applies to all group and phase velocity images.

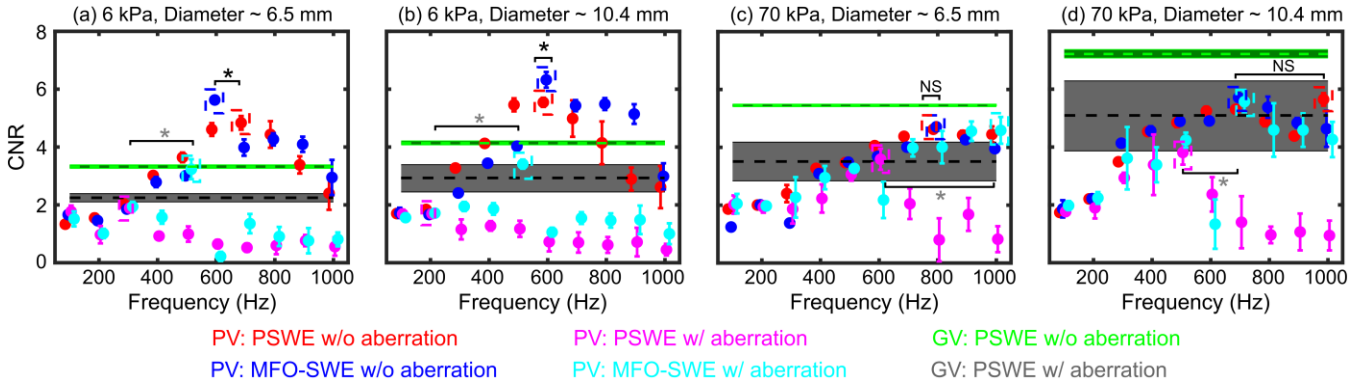

Fig 6, phantom: CNR of PSWE-derive group velocity (GV, green and black colors), PSWE (red and magenta) and MFO-SWE (blue and cyan colors)-derived phase velocity (PV) images of (a) 6.5 mm 6 kPa, (b) 10.4 mm 6 kPa, (c) 6.5 mm 70 kPa, and (d) 10.4 mm 70 kPa inclusions with and without the presence of an aberrating layer. Data are plotted as median ± 0.5*interquartile range over 7 repeated acquisitions. For (GV and PV) data, (dashed line and circular marker) and (shaded region and errorbar) represent the median and interquartile range, respectively. The Kruskal–Wallis test suggested that CNR of PSWE and MFO-SWE-derived PV images were statistically different across frequencies and dashed (blue or cyan) and (red or magenta) rectangles represent highest median CNR for MFO-SWE and PSWE, respectively. Black and grey asterisks represent statistically different PSWE and MFO-SWE-derived highest CNR (ranksum test) for without and with the presence of an aberrating layer. NS= Not significant;

SWE-PV-derived maximum CNR was significantly higher than PSWE-PV for both stiffer inclusions and GV for 6.5 mm, 70 kPa inclusion, respectively.

Fig. 7 shows representative B-mode, GV, and PV images derived by PSWE and MFO-SWE of a bovine liver *ex vivo* with and without aberration. Four observations are notable. First, PV in all frequencies except 100 and 200 Hz is lower than the GV irrespective of the method. Second, PV varied with frequency which was an indicator of the viscoelastic nature of the liver irrespective of methods or conditions. Third, PSWE-derived PV was higher than MFO-SWE for most frequencies. Fourth, MFO-SWE-derived PV images were more homogeneous than PSWE in higher frequencies (600-1000 Hz).

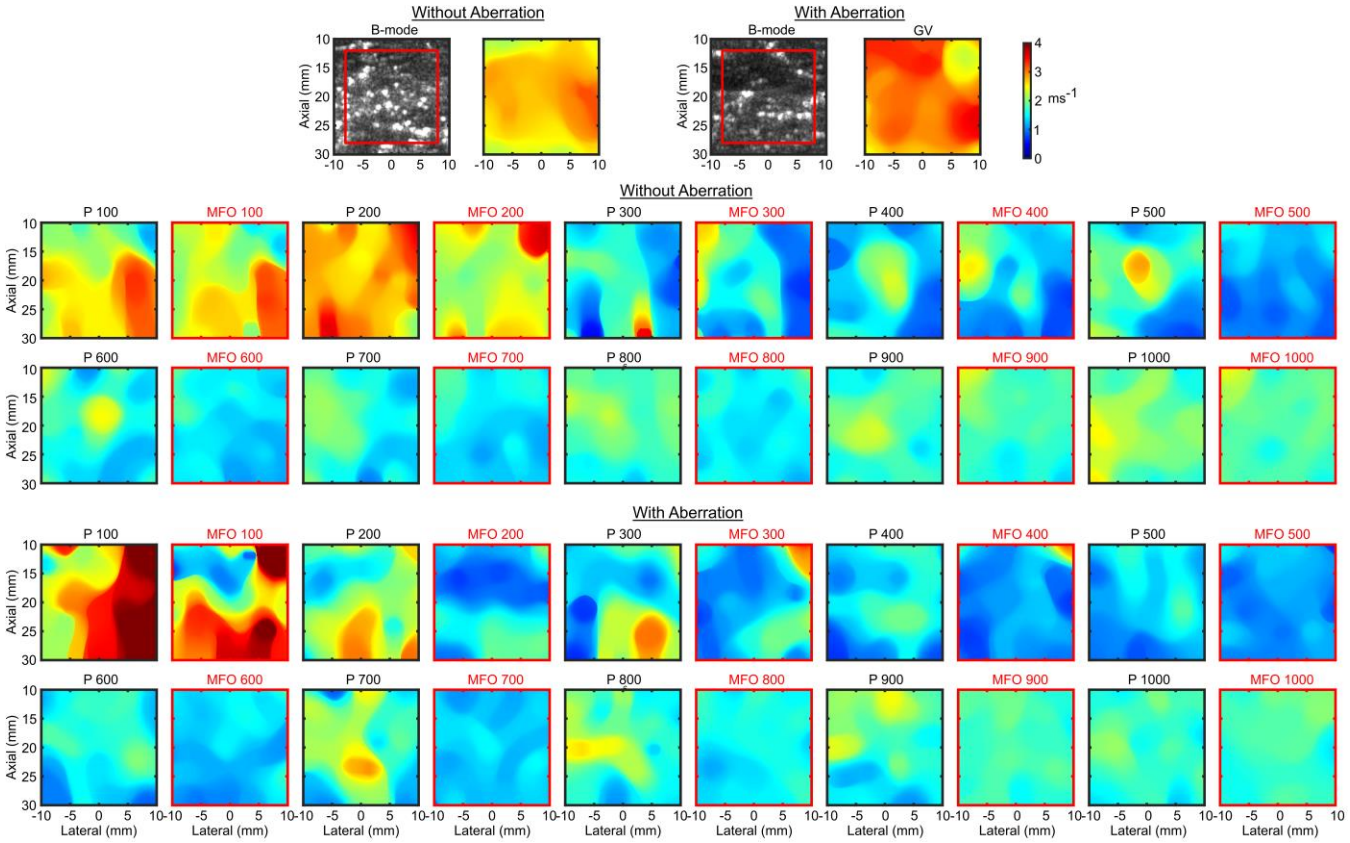

Fig 7, ex vivo bovine liver: B-mode, PSWE-derived group velocity (GV), PSWE and MFO-SWE-derived phase velocity (PV) images at 100-1000 Hz of the liver with and without the presence of an aberrating layer. B-mode and GV images are shown side-by-side at the 1st row. PSWE (denote by P) and MFO-SWE (denote by MFO) - derived PV image at each frequency are shown side-by-side at (2nd, 3rd) and (4th, 5th) rows for without and with the aberrating layer, respectively. The border and title of PSWE and MFO-SWE-derived PV images are in black versus red color for better distinction. The colorbar applies to all group and phase velocity images.

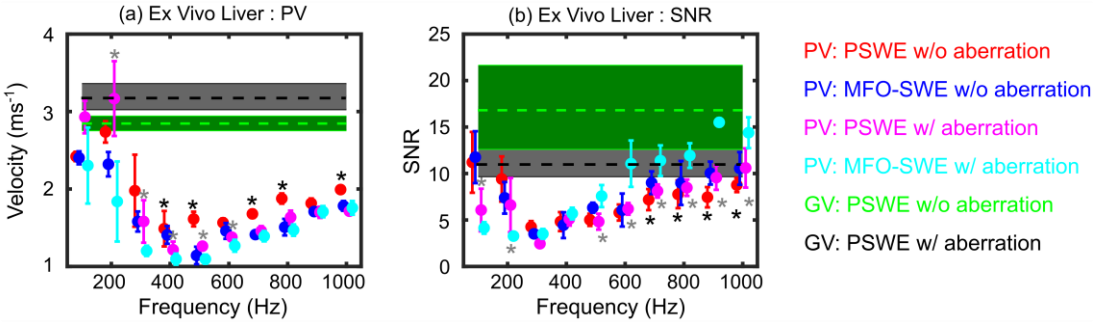

Fig 8, ex vivo bovine liver: (a) PSWE-derive group velocity (GV, green and black colors), PSWE (red and magenta) and MFO-SWE (blue and cyan colors)-derived phase velocity (PV) (b) SNR of PSWE and MFO-SWE images of ex vivo liver. Data are plotted as median ± 0.5*interquartile range over 7 repeated acquisitions. For (GV and PV) data, (dashed line and circular marker) and (shaded region and errorbar) represent the median and interquartile range, respectively. Black and grey asterisks represent statistically different (ranksum test) PSWE and MFO-SWE-derived PV and SNR for without and with the presence of an aberrating layer. Frequency without asterisk respresent not statistically significant SNR or PV between PSWE and MFO-SWE.

Fig.8 quantitatively compares the performance of PSWE and MFO-SWE in imaging *ex vivo* bovine liver in terms of velocity (panel a) and SNR (panel b). GV was significantly higher than PV at all frequencies except PSWE at 200 Hz irrespective of conditions. PSWE-derived PV was significantly higher than MFO-SWE at (400-500, 700-800, 1000) without aberration and at (200-600) Hz with aberration. GV-derived SNR was significantly higher than PSWE-PV at all frequencies except at 200, 900-1000 Hz (without aberration) and 100 Hz (with aberration), and MFO-SWE-PV at 100-800 Hz (without aberration) and 100-500 Hz (with aberration). MFO-SWE-PV-derived SNR was significantly higher than GV at 900-1000 Hz (with aberration) and higher than PSWE-PV at 700-1000 Hz (without aberration) and 500-1000 Hz (with aberration). PSWE-PV-derived SNR was significantly higher than MFO-SWE-PV only at 100 Hz without aberration.

Fig. 9 shows B-mode, GV, and PV images derived by PSWE and MFO-SWE of a chicken muscle at longitudinal and transverse orientation, *ex vivo*. Six observations are notable. First, both GV and PV were higher in longitudinal than transverse direction which was indicative of anisotropy in

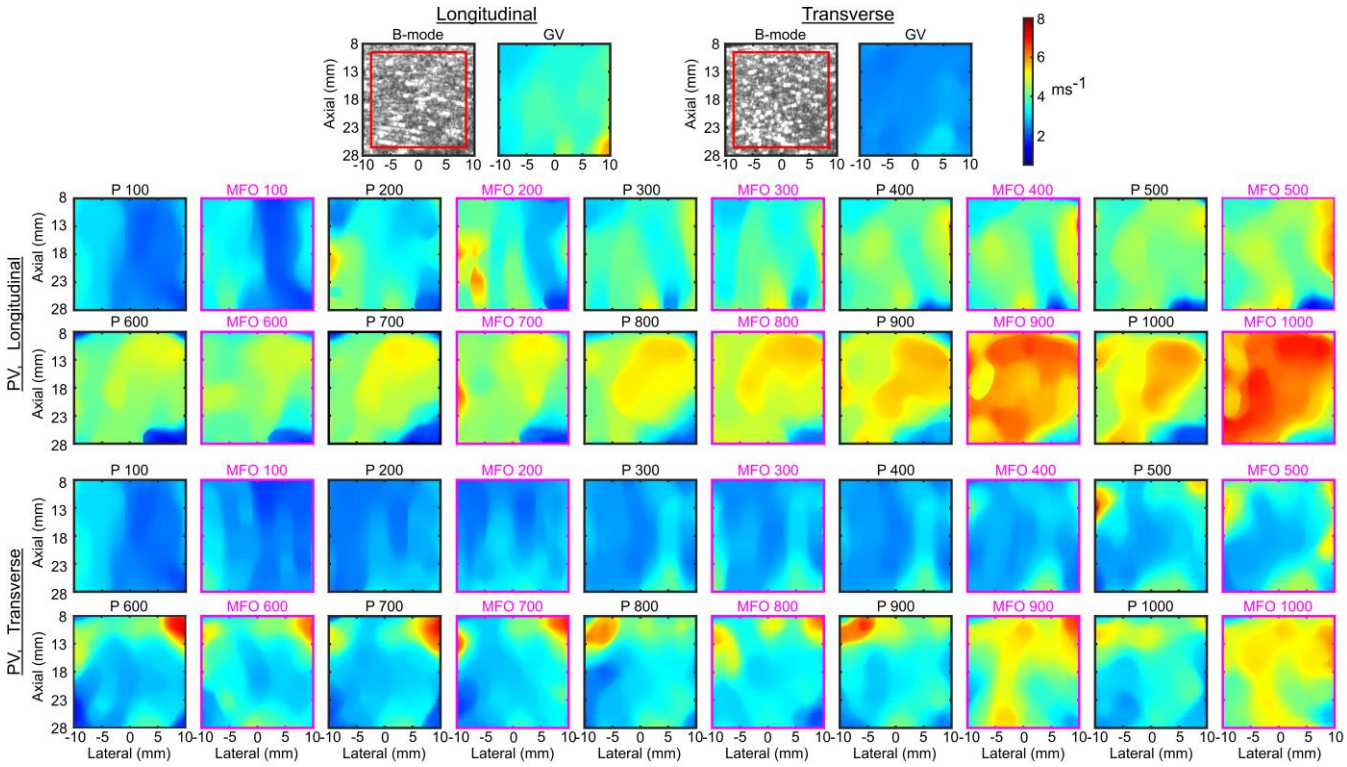

Fig 9, ex vivo chicken muscle: B-mode, PSWE-derive group velocity (GV), PSWE and MFO-SWE-derived phase velocity (PV) images at 100-1000 Hz of a chicken muscle at the longitudinal and transverse direction *ex vivo*. B-mode and GV images are shown side-by-side at the 1st row whereas PSWE (denote by P at the title) and MFO-SWE (denote by MFO at the title) -derived PV images at each frequency are shown side-by-side for longitudinal (2nd and 3rd row) and transverse (4th and 5th row) directions. The border and title of PSWE and MFO-SWE images are in black versus magenta color for better distinction. The red rectangle contour in the B-mode image represents the region of interest for median and SNR calculation. The colorbar applies to all GV and PV images.

Table II
PSWE-DERIVED MEDIAN GROUP VELOCITY (GV) AND PHASE VELOCITY (PV) AND MFO-SWE-DERIVED MEDIAN PV ALONG WITH SIGNAL TO NOISE RATIO (SNR) IN CHICKEN MUSCLE AT LONGITUDINAL AND TRANSVERSE DIRECTION.

Material	Metrics	Methods	GV	100	200	300	400	500	600	700	800	900	1000
Chicken Muscle Longitudinal	Med	PSWE	3.68	2.41	3.42	3.70	4.08	4.22	4.34	4.63	4.98	5.07	5.2
		MFO	--	2.90	3.58	3.65	4.11	4.38	4.31	4.42	4.91	5.85	6.27
	SNR	PSWE	14.7	6.8	6.9	9.5	11.6	12.7	9.0	7.6	8.5	8.4	6.8
		MFO	--	5.2	4.5	8.5	8.5	9.3	9.2	7.6	10.4	11.9	10.3
Chicken Muscle Transverse	Med	PSWE	2.51	2.32	2.50	2.60	268	2.97	3.0	3.02	3.3	3.42	3.57
		MFO	--	2.48	2.72	2.72	2.77	3.09	3.30	3.09	3.31	4.74	5.06
	SNR	PSWE	15.7	7.6	12.0	8.3	7.9	6.1	4.9	5.0	4.6	5.0	5.7
		MFO	--	7.5	9.3	8.8	9.9	5.5	6.3	5.6	5.6	7.3	10.5

viscoelastic properties. Second, PV increased with frequency in both orientations which indicates dispersion in PV. This dispersion may be due to the both viscoelastic and anisotropic natures of the chicken muscle. Third, PV at 400-1000 Hz was higher than the GV irrespective of methods. Fourth, both PSWE and MFO-SWE-derived PV images were more heterogeneous in transverse versus longitudinal directions. Fifth, at the longitudinal orientation, MFO-SWE-derived PV images were similar to the PSWE except at 900 and 1000 Hz. Sixth, at the transverse orientation, MFO-SWE-derived PV images were better homogeneous than PSWE at 600-1000 Hz. Table II lists the median and SNR of PV and GV images of chicken muscle at longitudinal and transverse orientations. At lower (100-500 Hz) and higher (600-1000 Hz) frequencies, the average percent difference in SNR between MFO-SWE and PSWE was (-20%, 4.4%) and (24%, 39%) in the (longitudinal, transverse) direction, respectively. The positive percent difference means MFO-SWE-derived SNR was higher than PSWE.

Fig. 10 shows B-mode, GV, PSWE, and MFO-SWE-derived PV images of a 4T1 mouse tumor, *in vivo*. Four observations are notable. First, PV images generally better delineated the tumor than GV. Second, PV was higher in the tumor than in neighboring tissue at most frequencies. Third, PV in the tumor increases with frequencies indicating that the mouse tumor is viscoelastic. Fourth, MFO-SWE-derived PV images better delineated the tumor than PSWE in most frequencies. The median PV and GV with CNR of the tumor

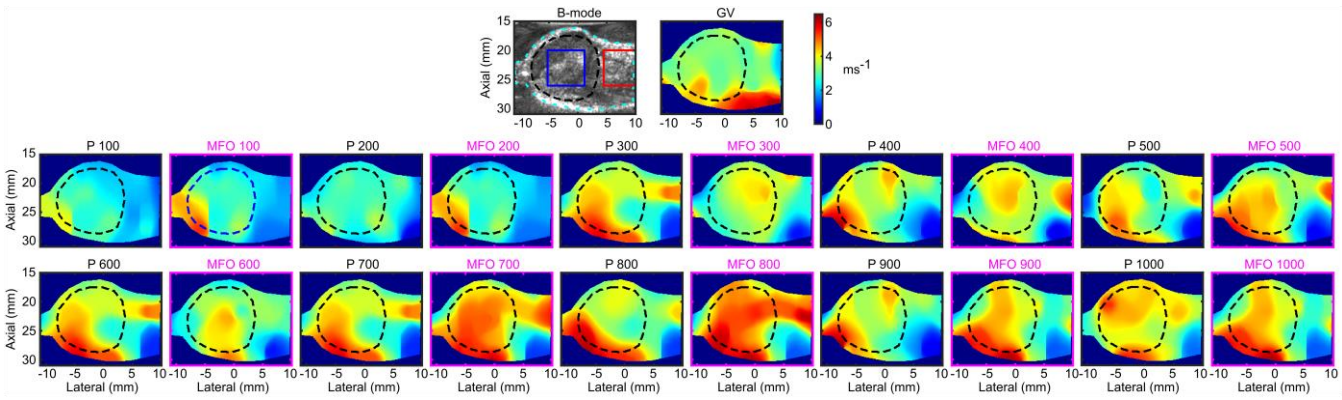

Fig 10, *in vivo* 4T1 mouse tumor: B-mode, PSWE-derive group velocity (GV), PSWE and MFO-SWE-derived particle velocity (PV) images at 100-1000 Hz of a tumor, *in vivo*. B-mode and GV images are shown side-by-side at the 1st row whereas PSWE (denote by P at the title) and MFO-SWE (denote by MFO at the title) -derived PV images at each frequency are shown side-by-side (2nd and 3rd row). The border and title of PSWE and MFO-SWE images are in black versus magenta color for better distinction. The dashed black, dashed green, blue, and red contours in the B-mode image represents tumor boundary, PV image field of view, the region of interest in tumor, and nearest non-cancerous tissue. The colorbar applies to all group and phase velocity images.

Table III
PSWE-DERIVED MEDIAN GROUP VELOCITY (GV) AND PHASE VELOCITY (PV) AND MFO-SWE-DERIVED MEDIAN PV ALONG WITH CNR IN MOUSE TUMOR AND NEIGHBORING NON-CANCEROUS (NC) TISSUE.

Material	Metrics	Methods	GV	100	200	300	400	500	600	700	800	900	1000
Tumor	Med	PSWE	3.24	2.69	2.84	3.03	3.57	4.00	4.08	3.87	3.57	3.84	4.33
		MFO	--	2.81	3.65	3.85	4.14	4.39	4.11	4.97	5.2	4.45	4.63
NC Tissue	Med	PSWE	3.21	1.94	2.29	2.72	2.63	3.52	282	3.65	3.28	3.35	3.63
		MFO	--	1.90	2.80	2.67	3.71	3.13	3.08	4.42	4.93	2.75	3.95
Tumor	CNR	PSWE	0.05	2.31	1.05	0.33	1.28	0.44	1.15	0.17	0.34	0.59	0.84
		MFO	--	2.40	1.19	2.14	0.47	1.08	1.95	0.56	0.21	2.62	0.89

are listed in Table III. CNR of the tumor in the MFO-SWE images was greater than 1.0 in all frequencies except 400, 600, and 700 Hz. However, PSWE-derived CNR was greater than 1.0 only at 100, 200, 400, and 600 Hz.

IV. DISCUSSION

This study presents a novel method, named MFO-SWE, to generate PV images at 100-1000 Hz via a single imaging transducer by inducing and tracking multi-frequency motion. While MFO-SWE-derived PVs at 100-1000 Hz were demonstrated in this study, the method can be expanded to generate PV images at other frequencies. As the PV image quality depends on the feature size, viscoelasticity, and frequency, the performance of MFO-SWE can be further improved by making the data collection in two steps. In the first step, the data can be collected in a wider frequency range (100-1500 Hz), then a narrow frequency range around the best-performing frequency that can be used in the second step.

In this study, MFO-SWE-derived PV images were compared against PSWE-derived PV and GV images. PSWE is considered a comparative benchmark rather than ground truth validation. There is a difference between PSWE versus MFO-SWE in terms of the intensity or energy of the excitation pulse. While the mechanical index was the same for both pulses (i.e., the voltage in the Verasonics system was kept the same between PSWE and MFO-SWE), the temporal intensity is higher in MFO-SWE. One way to increase the temporal intensity in PSWE is to increase the pulse duration. However, there is a limit to increasing the pulse duration due to the power supply and transducer hardware constraints. While 20 discrete excitation pulses (5 pulses per period and 4 cycles) were used in MFO-SWE, there was at least a 1.5 ms separation between two discrete pulses which enabled circumventing power supply and transducer hardware constraints and not crossing U.S. FDA limits. To evaluate the safety of MFO-SWE, acoustic pressure and intensity of the excitation pulses and temperature rise during the entire MFO-SWE sequence were measured using the method described in our previous work [45]. The acoustic pressure was measured in the water and was derated by assuming acoustic attenuation = 0.3 $dBcm^{-1}MHz^{-1}$. Using F-number = 2.0, focal depth = 25 mm, and Verasonics voltage = 40 V, the derated mechanical index ($MI_{0.3}$), spatial peak temporal average ($I_{SPTA,0.3}$), and spatial peak pulsed average ($I_{SPPA,0.3}$) of the proposed excitation pulse was 1.5, 37 Wm^{-2}, and 402 Wm^{-2}. Due to the separation of the discrete excitation pulses (Fig. 2), the temperature rise at the focal depth due to the entire MFO-SWE sequence was 0.6°C. The current U.S. FDA limits for $MI_{0.3}$ and tempera rise for diagnostic purposes were 1.9 and 6 °C, respectively [45], [49]. Therefore, MFO-SWE distributes excitation pulse energy at the target frequency without crossing FDA limits. Despite the longer pulse, motion artifacts do not challenge MFO-SWE as the frequency of oscillation is known and can easily be filtered out.

In addition to the assessment of the viscosity [6],

maximization of CNR is possible by generating PV images at different oscillation frequencies. While GV-derived CNR was more than PV in most frequencies, MFO-SWE-PV-derived maximum CNR of the softer inclusions without aberration, smaller inclusions with aberration, and mouse tumors was always higher than the GV (Fig. 6 and Tables III). This indicates that the detectability of inclusion can be improved by generating PV images at multiple frequencies especially difficult-to-image inclusions (i.e. smaller and softer inclusions). Note that, the Young's moduli ratio of inclusion to background (18 kPa) was lower for 6 kPa versus 70 kPa. The improvement in CNR by PV compared to GV is higher in the tumor than in elastic inclusions. Both PSWE and MFO-SWE-derived PV at 100 Hz were unable to detect the presence of either 6 or 70 kPa inclusion due to the higher shear wavelength associated with 100 Hz. Note that the shear wavelength of 6 kPa, 70 kPa (inclusion), and 18 kPa (background) at 100 Hz is 14.1 mm, 48.3 mm, and 24.5 mm, respectively assuming the density of the material is 1000 kgm^{-3}. As the wavelength of 100 Hz oscillation at 6 or 70 kPa is higher than the inclusion diameter, PV estimation at 100 Hz was corrupted and was higher than other frequencies. Whether PSWE or MFO-SWE was used, CNR was higher in 10.4 versus 6.5 mm diameter inclusions with the same stiffness (Figs. 6). This could be due to the discrepancy in the manufacturing process or better realizations of motion at a particular frequency in the larger inclusion. Without an aberration layer, MFO-SWE-PV derived maximum CNR was significantly higher than PSWE for both softer (6 kPa) inclusions only. This could be due to the effect of softer inclusion on the propagating shear waves or due to the lower Young's moduli ratio in the softer inclusion as discussed above. The shear wave is decelerated after entering the softer inclusion which may distort the higher frequency components. This may affect PSWE more than MFO-SWE because excitation pulse energy is distributed at the target frequencies with higher weights to the higher frequencies in the MFO-SWE.

With the presence of the aberration layer, MFO-SWE-PV derived maximum CNR was significantly higher than PSWE for all inclusions. At 600-1000 Hz, MFO-SWE improved the CNR of inclusions on an average of 8.2% versus 156% for without versus with the presence of pork abdominal layer compared to the PSWE. The presence of a pork abdominal layer impacts the PV imaging by reducing the echo SNR, introducing phase aberration and attenuated ARF magnitude which affect the generation and tracking of ARF-induced motion. The echo SNR of the tracking pulses was calculated as $20 \log_{10}(\mu / \sigma)$ over the same field of view of the PV image where μ and σ are the mean and standard deviation of the beamformed envelope signals over the reference frames [51]. The average echo SNR of the phantom with and without the aberration layer was 38 and 31 dB. The presence of dispersion in softer versus stiffer inclusion was also different. The dispersion can be quantified by using dispersion slope (DS) with higher DS means higher viscosity [5]. The DS is calculated by fitting PV versus frequency (400-1000 Hz) with linear regression. The average DS was similar in the background of softer (-0.3 versus -0.1 $ms^{-1}kHz^{-1}$) and stiffer (-0.1 versus -0.2 $ms^{-1}kHz^{-1}$) for (without versus with) aberration layer. In contrast, the average DS varied from (0.3 versus 0.4) to (1.6 versus 0.6) $ms^{-1}kHz^{-1}$ in the softer to stiffer inclusion for (without versus with) aberration layer. Future investigation is needed to find out the source (viscosity and/or deceleration of shear wave speed) for worse boundary delineation (or CNR) by PSWE compared to MFO-SWE in the softer versus stiffer inclusion without aberration layer.

While the phantom is the idealistic representation of biological tissue, Figs, 7-10 and Tables II-III compare the performance of MFO-SWE versus PSWE to generate PV images in biological tissues. In the liver, PSWE-derived PV was significantly higher than MFO-SWE at several frequencies (Fig. 8a). The mean percent difference in MFO-SWE versus PSWE-derived median PV was (-15.2, -21.4) % and (-10.6, -4.7) % at 100-500 and 600-1000 Hz for (without, with) aberration, respectively. Note, a negative percent difference means MFO-SWE-derived PV is lower than the PSWE. Despite PSWE-derived PV being higher than MFO-SWE, MFO-SWE-derived SNR was significantly higher than PSWE at several frequencies (Fig. 8b). MFO-SWE improved SNR of PV images on an average (-7.9, 11.4) % and (20.3, 40.8) % at 100-500 and 600-1000 Hz for (without, with) aberration, respectively. The MFO-SWE provides higher SNR for higher frequencies as the energy is concentrated at target frequencies. Note, the higher SNR indicates better homogeneity in the image with an assumption that the bovine liver is mechanically homogeneous. If we observe more closely, we can see that the high and low pixel values within an image vary between frequencies and methods (Fig. 7). This indicates that lower SNR in PSWE compared to MFO-SWE (Fig. 8) may not be due to the presence of inhomogeneities in tissues but instead attributed to noise or loss associated with shear wave propagation impacting PV images differently at a different frequency and a different location on the propagation path. Note, the average (PSWE versus MFO-SWE)-derived DS was (0.6 versus 0.8) and (0.8 versus 1.3) for without versus with aberration layer, respectively. Both methods indicate higher DS for with versus without aberration. The presence of a pork layer in between the transducer surface and the liver may induce pressure that may alter the viscoelastic properties of the liver. Note, PSWE-derived GV was higher for with versus without aberration, respectively (Fig. 8a). One interesting observation is that PV-derived SNR was on an average 6.1 dB versus 9.6 dB at 100-500 versus 600-1000 Hz after combing both methods and conditions (Fig. 8b). At first, it seems counterintuitive as the higher loss is associated with higher frequency. However, it is important to note that the window for calculating PV was fixed at 4 x 4 mm^2 for all frequencies. Therefore, the higher portion of wavelength is contained in the window for the higher than lower frequencies.

While PV increases with frequency in both longitudinal and transverse directions in the chicken muscle (Fig. 9), the (PSWE, MFO-SWE)-derived DS was (2.0, 3.6) and (1.4, 3.6) $ms^{-1}kHz^{-1}$ in longitudinal and transverse direction,

respectively. The higher discrepancy between PSWE and MFO-SWE in the transverse direction may be due to the higher heterogeneity in the PSWE versus MFO-SWE. Note, the average percent difference in SNR between MFO-SWE and PSWE was (-24.6%, and -0.4%) and (23%, and 38.6%) in (longitudinal and transverse) directions for 100-500 and 600-1000 Hz, respectively. The SNR difference between MFO-SWE and PSWE at higher versus lower frequency may be due to the concentration of higher energy in the higher frequency of the excitation pulse in MFO-SWE and vice versa compared to the PSWE. Future studies will investigate the impact of energy difference in PSWE versus MFO-SWE excitation pulse on the SNR of PV images in the simulation framework. Irrespective of the method, PV images were more heterogeneous in transverse versus longitudinal direction. Future investigation is needed to study the effect of anisotropy in PV calculation in both longitudinal and transverse directions. Interestingly, the ratio of PV in longitudinal over transverse directions varied with the frequency. The higher ratio was observed around 400-800 Hz. Previously, it was shown that the shear wave dispersion vibrometry-derived PV ratio was variable with frequency in the anisotropic media [50].

For tumor imaging *in vivo*, MFO-SWE-derived PV images delineated tumor better than PSWE (Fig. 10) which is also corroborated by higher CNR of MFO-SWE images (Table III). Interestingly, PSWE-derived GV was unable to delineate the tumor. It may be due to the difference in viscosity of the tumor versus neighboring tissue or motion artifacts. Note, data was collected without any breath-gating. However, PSWE-derived PV was less affected by the motion artifacts as the PV is calculated at a particular frequency. In addition, less spatial overlap between generated PV images from two different excitation beam lateral focus locations (-7.5 and 8.5 mm) at two frames also impacted the PV images derived using both methods. Future studies will investigate the impact of the excitation beam focus location on PV images. Note, the (PSWE, MFO-SWE)-derived DS was (0.5, 1.0) and (1.1, 0.65) $ms^{-1}kHz^{-1}$ in the tumor and non-cancerous tissue, respectively.

The improvement in PV estimation at higher frequencies by MFO-SWE varied between the materials tested. The difference in improvement may not be due to the difference in echo SNR. Note that echo SNR will impact the phase velocity images by affecting the motion tracking. The average echo SNR of the liver (without and with aberration), muscle, and mouse tumor was (32.5 and 25.1), 29.4, and 34.2 dB, respectively. While the echo SNR was similar between different tissues (average 30.3 dB) and phantom (34.5 dB), the performance difference between PSWE and MFO-SWE was mainly due to the loss of shear wave energy associated with the viscosity of the tissue. In more highly viscous material, the shear waves will attenuate more and the reconstruction of phase velocity at a higher frequency will be noisier.

While this feasibility study of generating PV images using an MFO-SWE demonstrated strong promise, it has five main limitations. First, only one example of MFO-EP with m^2 weight (equation (1)) and 5 discrete excitation pulses per period was demonstrated. The weighting scheme, location, and the number of discrete pulses were selected empirically so that each frequency contains sufficient energy to generate motion above the noise level. The performance of MFO-SWE will vary based on the weighting scheme, selection of discrete excitation pulse, and viscoelasticity of tissues. While it is possible to optimize the weighting scheme and selection of discrete excitation pulse based on the imaging condition, the proposed excitation pulse generated PV images of the phantom, liver, chicken muscle, and mouse tumor which demonstrates the applicability of the proposed pulse for imaging diverse tissues. Future studies will explore the feasibility of optimizing the weighting scheme and selection of discrete excitation pulse based on the imaging condition by comparing different pulse sequences in simulated material or two-step data collection mentioned previously. Second, while the difference in PSWE and MFO-SWE-derived median PV was less than 10% in most frequencies and imaged materials (Tables II-III, Fig. 8), there was no validation of which PV was correct. Future studies will explore the use of different simulation methods to compare PSWE and MFO-SWE-derived PV in heterogeneous media. Third, PVs were estimated without estimation of viscoelasticity. As the viscoelasticity assessment depends on the PV estimation, we expect that MFO-SWE will provide a better viscoelasticity estimation compared to the PSWE. However, estimation of viscoelasticity depends on the selection of materials models [52], [53]. An appropriate model for the MFO-SWE-derived PV dispersion relationship will be explored in the future and will be compared with PSWE-derived viscoelasticity in the presence of an aberration layer, reverberation noise, and motion artifacts. In addition to viscoelasticity estimation, PV at each frequency has the potential to be used as a biomarker and can be used in artificial intelligence algorithms to improve diagnosis. Fourth, SNR was used to compare the performance of PSWE and MFO-SWE in the liver and chicken muscle with as assumption that both tissues are mechanically homogeneous. There was no histopathological validation for this assumption. Fifth, MFO-SWE is demonstrated for only one *in vivo* case without any human imaging. Future studies will investigate the applicability of MFO-SWE for tumor imaging in breast cancer patients.

V. Conclusion

This study demonstrated the feasibility of an MFO excitation pulse to generate PV images at 100-1000 Hz using a single imaging transducer. The MFO excitation pulse is composed of a sum of sinusoids with higher weights to higher frequencies. The feasibility of MFO-SWE was demonstrated by imaging 4 inclusions, excised bovine liver and chicken muscle, and *in vivo* 4T1 mouse breast tumor. The median percent difference in PV between MFO-SWE versus PSWE was less than 10% in most cases. However, the MFO-SWE achieved higher CNR in inclusions and tumors and higher SNR in liver and chicken muscles. The MFO-SWE achieved a significant improvement in PV imaging over PSWE when there was a presence of an aberration layer between the

transducer and imaging medium. The main advantage of MFO-SWE over alternate methods is its ability to distribute the energy over target frequencies to improve the PV estimation in the corresponding frequencies. Overall, this study demonstrated a new SWE-based method to assess PV of tissue which shows promise for future clinical applications.

ACKNOWLEDGMENTS

The authors thank Drs. Saurabh Singh, Indranil Basu, and Chandan Guha from the Albert Einstein College of Medicine & Montefiore Medical Center for providing the 4T1 cells, and Xiaoyue Li for the help in the mouse experiments.

REFERENCES

[1] R. M. S. Sigrist, J. Liau, A. El Kaffas, M. C. Chammas, and J. K. Willmann, "Ultrasound Elastography: Review of Techniques and Clinical Applications," *Theranostics*, vol. 7, no. 5, pp. 1303–1329, 2017, doi: 10.7150/thno.18650.

[2] Y.-C. Fung, *Mechanical Properties of Living Tissues*, 2nd ed. New York, NY: Springer New York, 1993. doi: 10.1007/978-1-4757-2257-4.

[3] K. J. Parker, J. Ormachea, and Z. Hah, "Group versus Phase Velocity of Shear Waves in Soft Tissues," *Ultrason. Imaging*, vol. 40, no. 6, pp. 343–356, Nov. 2018, doi: 10.1177/0161734618796217.

[4] Y. Zhu *et al.*, "The Role of Viscosity Estimation for Oil-in-gelatin Phantom in Shear Wave Based Ultrasound Elastography," *Ultrasound Med. Biol.*, vol. 41, no. 2, pp. 601–609, Feb. 2015, doi: 10.1016/j.ultrasmedbio.2014.09.028.

[5] K. Nightingale *et al.*, "Derivation and analysis of viscoelastic properties in human liver: Impact of frequency on fibrosis and steatosis staging," *IEEE Trans. Ultrason. Ferroelectr. Freq. Control*, vol. 62, no. 1, pp. 165–175, 2015, doi: 10.1109/TUFFC.2014.006653.

[6] T. Deffieux, G. Montaldo, M. Tanter, and M. Fink, "Shear wave spectroscopy for in vivo quantification of human soft tissues visco-elasticity," *IEEE Trans. Med. Imaging*, vol. 28, no. 3, pp. 313–322, 2009, doi: 10.1109/TMI.2008.925077.

[7] S. Chen *et al.*, "Assessment of liver viscoelasticity by using shear waves induced by ultrasound radiation force.," *Radiology*, vol. 266, no. 3, pp. 964–70, Mar. 2013, doi: 10.1148/radiol.12120837.

[8] N. Salameh *et al.*, "Hepatic viscoelastic parameters measured with MR elastography: Correlations with quantitative analysis of liver fibrosis in the rat," *J. Magn. Reson. Imaging*, vol. 26, no. 4, pp. 956–962, Oct. 2007, doi: 10.1002/jmri.21099.

[9] Y. Qiu, M. Sridhar, J. K. Tsou, K. K. Lindfors, and M. F. Insana, "Ultrasonic Viscoelasticity Imaging of Nonpalpable Breast Tumors," *Acad. Radiol.*, vol. 15, no. 12, pp. 1526–1533, Dec. 2008, doi: 10.1016/j.acra.2008.05.023.

[10] R. Sinkus *et al.*, "Imaging anisotropic and viscous properties of breast tissue by magnetic resonance-elastography.," *Magn. Reson. Med.*, vol. 53, no. 2, pp. 372–87, Feb. 2005, doi: 10.1002/mrm.20355.

[11] V. Kumar *et al.*, "Viscoelastic parameters as discriminators of breast masses: Initial human study results.," *PLoS One*, vol. 13, no. 10, p. e0205717, 2018, doi: 10.1371/journal.pone.0205717.

[12] J.-L. L. Gennisson, T. Deffieux, E. Macé, G. Montaldo, M. Fink, and M. Tanter, "Viscoelastic and anisotropic mechanical properties of in vivo muscle tissue assessed by supersonic shear imaging.," *Ultrasound Med. Biol.*, vol. 36, no. 5, pp. 789–801, May 2010, doi: 10.1016/j.ultrasmedbio.2010.02.013.

[13] K. Hoyt, T. Kneezel, B. Castaneda, and K. J. Parker, "Quantitative sonoelastography for the in vivo assessment of skeletal muscle viscoelasticity," *Phys. Med. Biol.*, vol. 53, no. 15, pp. 4063–4080, Aug. 2008, doi: 10.1088/0031-9155/53/15/004.

[14] C. J. Moore *et al.*, "In Vivo Viscoelastic Response (VisR) Ultrasound for Characterizing Mechanical Anisotropy in Lower-Limb Skeletal Muscles of Boys with and without Duchenne Muscular Dystrophy," *Ultrasound Med. Biol.*, vol. 44, no. 12, pp. 2519–2530, Aug. 2018, doi: 10.1016/j.ultrasmedbio.2018.07.004.

[15] M. M. Hossain *et al.*, "Evaluating Renal Transplant Status Using Viscoelastic Response (VisR) Ultrasound.," *Ultrasound Med. Biol.*, vol. 44, no. 8, pp. 1573–1584, May 2018, doi: 10.1016/j.ultrasmedbio.2018.03.016.

[16] C. Amador, M. W. Urban, S. Chen, and J. F. Greenleaf, "Shearwave dispersion ultrasound vibrometry (SDUV) on swine kidney," *IEEE Trans. Ultrason. Ferroelectr. Freq. Control*, vol. 58, no. 12, pp. 2608–2619, 2011, doi: 10.1109/TUFFC.2011.2124.

[17] M. W. Urban, S. Chen, and M. Fatemi, "A Review of Shearwave Dispersion Ultrasound Vibrometry (SDUV) and its Applications," *Curr. Med. Imaging Rev.*, vol. 8, no. 1, pp. 27–36, Feb. 2012, doi: 10.2174/157340512799220625.

[18] A. Arani, A. Manduca, R. L. Ehman, and J. Huston Iii, "Harnessing brain waves: a review of brain magnetic resonance elastography for clinicians and scientists entering the field.," *Br. J. Radiol.*, vol. 94, no. 1119, p. 20200265, Mar. 2021, doi: 10.1259/bjr.20200265.

[19] F. Viola and W. F. Walker, "Radiation force imaging of viscoelastic properties with reduced artifacts.," *IEEE Trans. Ultrason. Ferroelectr. Freq. Control*, vol. 50, no. 6, pp. 736–42, Jun. 2003, Accessed: Aug. 28, 2016. [Online]. Available: http://www.ncbi.nlm.nih.gov/pubmed/10870702

[20] X. Zhao and A. a. Pelegri, "Dynamic Simulation of Viscoelastic Soft Tissue in Acoustic Radiation Force Creep Imaging," *J. Biomech. Eng.*, vol. 136, no. 9, p. 094502, 2014, doi: 10.1115/1.4027934.

[21] M. M. Hossain and C. M. Gallippi, "Viscoelastic Response Ultrasound Derived Relative Elasticity and Relative Viscosity Reflect True Elasticity and Viscosity: In Silico and Experimental Demonstration.," *IEEE Trans. Ultrason. Ferroelectr. Freq. Control*, vol. 67, no. 6, pp. 1102–1117, 2020, doi: 10.1109/TUFFC.2019.2962789.

[22] M. Bhatt *et al.*, "Reconstruction of Viscosity Maps in Ultrasound Shear Wave Elastography.," *IEEE Trans. Ultrason. Ferroelectr. Freq. Control*, vol. 66, no. 6, pp. 1065–1078, Apr. 2019, doi: 10.1109/TUFFC.2019.2908550.

[23] S. Chen *et al.*, "Shearwave dispersion ultrasound vibrometry (SDUV) for measuring tissue elasticity and viscosity.," *IEEE Trans. Ultrason. Ferroelectr. Freq. Control*, vol. 56, no. 1, pp. 55–62, Jan. 2009, doi: 10.1109/TUFFC.2009.1005.

[24] I. Z. Nenadic *et al.*, "Application of Attenuation Measuring Ultrasound Shearwave Elastography in 8 post-transplant liver patients," *IEEE Int. Ultrason. Symp. IUS*, no. 1, pp. 987–990, 2014, doi: 10.1109/ULTSYM.2014.0242.

[25] N. C. Rouze, M. L. Palmeri, and K. R. Nightingale, "An analytic, Fourier domain description of shear wave propagation in a viscoelastic medium using asymmetric Gaussian sources.," *J. Acoust. Soc. Am.*, vol. 138, no. 2, pp. 1012–22, Aug. 2015, doi: 10.1121/1.4927492.

[26] S. Kazemirad, S. Bernard, S. Hybois, A. Tang, and G. Cloutier, "Ultrasound Shear Wave Viscoelastography: Model-Independent Quantification of the Complex Shear Modulus.," *IEEE Trans. Ultrason. Ferroelectr. Freq. Control*, vol. 63, no. 9, pp. 1399–1408, Sep. 2016, doi: 10.1109/TUFFC.2016.2583785.

[27] E. Budelli *et al.*, "A diffraction correction for storage and loss moduli imaging using radiation force based elastography.," *Phys. Med. Biol.*, vol. 62, no. 1, pp. 91–106, 2017, doi: 10.1088/1361-6560/62/1/91.

[28] P. Kijanka and M. W. Urban, "Local Phase Velocity Based Imaging: A New Technique Used for Ultrasound Shear Wave Elastography.," *IEEE Trans. Med. Imaging*, vol. 38, no. 4, pp. 894–908, Apr. 2019, doi: 10.1109/TMI.2018.2874545.

[29] P. Kijanka and M. W. Urban, "Local Phase Velocity Based Imaging (LPVI) of Viscoelastic Phantoms and Tissues," *IEEE Trans. Ultrason. Ferroelectr. Freq. Control*, vol. 3010, no. c, pp. 1–1, 2020, doi: 10.1109/TUFFC.2020.2968147.

[30] J. Vappou, C. Maleke, and E. E. Konofagou, "Quantitative viscoelastic parameters measured by harmonic motion imaging," *Phys. Med. Biol.*, vol. 54, no. 11, pp. 3579–3594, Jun. 2009, doi: 10.1088/0031-9155/54/11/020.

[31] C. Amador, M. W. Urban, S. Chen, and J. F. Greenleaf, "Loss tangent and complex modulus estimated by acoustic radiation force creep and shear wave dispersion.," *Phys Med Biol*, vol. 57, no. 5, pp. 1263–82, Mar. 2012, doi: 10.1088/0031-9155/57/5/1263.

[32] S. Catheline *et al.*, "Measurement of viscoelastic properties of homogeneous soft solid using transient elastography: An inverse problem approach," *J. Acoust. Soc. Am.*, vol. 116, no. 6, pp. 3734–3741, Dec. 2004, doi: 10.1121/1.1815075.

[33] S. Bernard, S. Kazemirad, and G. Cloutier, "A Frequency-Shift Method to Measure Shear-Wave Attenuation in Soft Tissues.," *IEEE Trans. Ultrason. Ferroelectr. Freq. Control*, vol. 64, no. 3, pp. 514–524, 2017, doi: 10.1109/TUFFC.2016.2634329.

[34] J. Bercoff, M. Tanter, M. Muller, and M. Fink, "The role of viscosity in the impulse diffraction field of elastic waves induced by the acoustic radiation force.," *IEEE Trans. Ultrason. Ferroelectr. Freq. Control*, vol.

51, no. 11, pp. 1523–36, Nov. 2004, doi: 10.1109/TUFFC.2004.1367494.

[35] J. H. Langdon, E. Elegbe, and S. A. McAleavey, “Single tracking location acoustic radiation force impulse viscoelasticity estimation (STL-VE): A method for measuring tissue viscoelastic parameters.,” *IEEE Trans. Ultrason. Ferroelectr. Freq. Control*, vol. 62, no. 7, pp. 1225–44, Jul. 2015, doi: 10.1109/TUFFC.2014.006775.

[36] R. J. G. van Sloun, R. R. Wildeboer, H. Wijkstra, and M. Mischi, “Viscoelasticity Mapping by Identification of Local Shear Wave Dynamics,” *IEEE Trans. Ultrason. Ferroelectr. Freq. Control*, vol. 64, no. 11, pp. 1666–1673, Nov. 2017, doi: 10.1109/TUFFC.2017.2743231.

[37] M. R. Selzo, C. J. Moore, M. M. Hossain, M. L. Palmeri, and C. M. Gallippi, “On the Quantitative Potential of Viscoelastic Response (VisR) Ultrasound Using the One-Dimensional Mass-Spring-Damper Model.,” *IEEE Trans. Ultrason. Ferroelectr. Freq. Control*, vol. 63, no. 9, pp. 1276–87, 2016, doi: 10.1109/TUFFC.2016.2539323.

[38] S. Sadeghi, C.-Y. Lin, and D. H. Cortes, “Narrowband Shear Wave Generation Using Sinusoidally Modulated Acoustic Radiation Force,” *IEEE Trans. Ultrason. Ferroelectr. Freq. Control*, vol. 66, no. 2, pp. 264–272, Feb. 2019, doi: 10.1109/TUFFC.2018.2884847.

[39] Y. Zheng *et al.*, “Ultrasound vibrometry using orthogonal-frequency-based vibration pulses,” *IEEE Trans. Ultrason. Ferroelectr. Freq. Control*, vol. 60, no. 11, pp. 2359–2370, 2013, doi: 10.1109/TUFFC.2013.6644739.

[40] A. Nabavizadeh, T. Payen, N. Saharkhiz, M. McGarry, K. P. Olive, and E. E. Konofagou, “Technical Note: In vivo Young’s modulus mapping of pancreatic ductal adenocarcinoma during HIFU ablation using harmonic motion elastography (HME),” *Med. Phys.*, vol. 45, no. 11, pp. 5244–5250, 2018, doi: 10.1002/mp.13170.

[41] H. Zhao *et al.*, “External vibration multi-directional ultrasound shearwave elastography (EVMUSE): application in liver fibrosis staging.,” *IEEE Trans. Med. Imaging*, vol. 33, no. 11, pp. 2140–8, Nov. 2014, doi: 10.1109/TMI.2014.2332542.

[42] Yi Zheng *et al.*, “Ultrasound vibrometry using orthogonal- frequency-based vibration pulses,” *IEEE Trans. Ultrason. Ferroelectr. Freq. Control*, vol. 60, no. 11, pp. 2359–2370, Nov. 2013, doi: 10.1109/TUFFC.2013.6644739.

[43] M. M. Hossain and E. Konofagou, “Phase velocity imaging using acoustic radiation force-induced shear wave with a multi-frequency excitation pulse,” *J. Acoust. Soc. Am.*, vol. 150, no. 4, pp. A289–A289, Oct. 2021, doi: 10.1121/10.0008321.

[44] P. Song, A. Manduca, H. Zhao, M. W. Urban, J. F. Greenleaf, and S. Chen, “Fast shear compounding using directional filtering and two-dimensional shear wave speed calculation,” *IEEE Int. Ultrason. Symp. IUS*, pp. 1264–1267, 2013, doi: 10.1109/ULTSYM.2013.0323.

[45] M. M. Hossain, N. Saharkhiz, and E. E. Konofagou, “Feasibility of Harmonic Motion Imaging Using a Single Transducer: In Vivo Imaging of Breast Cancer in a Mouse Model and Human Subjects,” *IEEE Trans. Med. Imaging*, vol. 40, no. 5, pp. 1390–1404, May 2021, doi: 10.1109/TMI.2021.3055779.

[46] T. Savage, S. Pandey, and C. Guha, “Postablation Modulation after Single High-Dose Radiation Therapy Improves Tumor Control via Enhanced Immunomodulation,” *Clin. Cancer Res.*, vol. 26, no. 4, pp. 910–921, Feb. 2020, doi: 10.1158/1078-0432.CCR-18-3518.

[47] A. Manduca, D. S. Lake, S. A. Kruse, and R. L. Ehman, “Spatio-temporal directional filtering for improved inversion of MR elastography images,” *Med. Image Anal.*, vol. 7, no. 4, pp. 465–473, 2003, doi: 10.1016/S1361-8415(03)00038-0.

[48] P. J. Hollender, S. J. Rosenzweig, K. R. Nightingale, and G. E. Trahey, “Single- and Multiple-Track-Location Shear Wave and Acoustic Radiation Force Impulse Imaging: Matched Comparison of Contrast, Contrast-to-Noise Ratio and Resolution,” *Ultrasound Med. Biol.*, vol. 41, no. 4, pp. 1043–1057, 2015, doi: 10.1016/j.ultrasmedbio.2014.11.006.

[49] P. Song, H. Zhao, A. Manduca, M. W. Urban, J. F. Greenleaf, and S. Chen, “Comb-Push Ultrasound Shear Elastography (CUSE): A Novel Method for Two-Dimensional Shear Elasticity Imaging of Soft Tissues,” *IEEE Trans. Med. Imaging*, vol. 31, no. 9, pp. 1821–1832, Sep. 2012, doi: 10.1109/TMI.2012.2205586.

[50] M. W. Urban, B. Qiang, P. Song, I. Z. Nenadic, S. Chen, and J. F. Greenleaf, “Investigation of the effects of myocardial anisotropy for shear wave elastography using impulsive force and harmonic vibration,” *Phys. Med. Biol.*, vol. 61, no. 1, pp. 365–382, Jan. 2016, doi: 10.1088/0031-9155/61/1/365.

[51] H.-W. Xie, H. Guo, G.-Q. Zhou, N. Q. Nguyen, and R. W. Prager, “Improved ultrasound image quality with pixel-based beamforming using a Wiener-filter and a SNR-dependent coherence factor.,” *Ultrasonics*, vol. 119, no. February 2021, p. 106594, Feb. 2022, doi: 10.1016/j.ultras.2021.106594.

[52] C. A. Trutna, N. C. Rouze, M. L. Palmeri, and K. R. Nightingale, “Measurement of Viscoelastic Material Model Parameters using Fractional Derivative Group Shear Wave Speeds in Simulation and Phantom Data,” *IEEE Trans. Ultrason. Ferroelectr. Freq. Control*, vol. PP, no. c, pp. 1–1, 2019, doi: 10.1109/TUFFC.2019.2944126.

[53] L. M. Wiseman, M. W. Urban, and R. J. McGough, “A parametric evaluation of shear wave speeds estimated with time-of-flight calculations in viscoelastic media,” *J. Acoust. Soc. Am.*, vol. 148, no. 3, pp. 1349–1371, Sep. 2020, doi: 10.1121/10.0001813.